

## RESEARCH ARTICLE

10.1002/2014JB011227

## Key Points:

- We provide InSAR constraints on an induced earthquake
- There is a strong correlation between anthropogenic deformation and seismicity
- InSAR will be a valuable tool in monitoring induced seismicity

## Supporting Information:

- Readme
- Figure S1
- Figure S2
- Figure S3
- Figure S4
- Figure S5

## Correspondence to:

W. D. Barnhart,  
wbarnhart@usgs.gov

## Citation:

Barnhart, W. D., H. M. Benz, G. P. Hayes, J. L. Rubinstein, and E. Bergman (2014), Seismological and geodetic constraints on the 2011  $M_w$ 5.3 Trinidad, Colorado earthquake and induced deformation in the Raton Basin, *J. Geophys. Res. Solid Earth*, 119, doi:10.1002/2014JB011227.

Received 24 APR 2014

Accepted 22 SEP 2014

Accepted article online 27 SEP 2014

## Seismological and geodetic constraints on the 2011 $M_w$ 5.3 Trinidad, Colorado earthquake and induced deformation in the Raton Basin

W. D. Barnhart<sup>1</sup>, H. M. Benz<sup>1</sup>, G. P. Hayes<sup>1</sup>, J. L. Rubinstein<sup>2</sup>, and E. Bergman<sup>3</sup>

<sup>1</sup>U.S. Geological Survey Geologic Hazards Science Center, Golden, Colorado, USA, <sup>2</sup>U.S. Geological Survey Earthquake Science Center, Menlo Park, California, USA, <sup>3</sup>Global Seismological Services, Golden, Colorado, USA

**Abstract** The Raton Basin of southern Colorado and northern New Mexico is an actively produced hydrocarbon basin that has experienced increased seismicity since 2001, including the August 2011  $M_w$ 5.3 Trinidad normal faulting event. Following the 2011 earthquake, regional seismic observations were used to relocate 21 events, including the 2011 main shock, two foreshocks, and 13 aftershocks. Additionally, interferometric synthetic aperture radar (InSAR) observations of both the 2011 event and preevent basin deformation place constraint on the spatial kinematics of the 2011 event and localized basin subsidence due to ground water or gas withdrawal. We find that the 2011 earthquake ruptured an 8–10 km long segment of a normal fault at depths of 1.5–6.0 km within the crystalline Precambrian basement underlying the Raton Basin sedimentary rocks. The earthquake also nucleated within the crystalline basement in the vicinity of an active wastewater disposal site. The ensuing aftershock sequence demonstrated statistical properties expected for intraplate earthquakes, though the length of the 2011 earthquake is unexpectedly long for an  $M_w$ 5.3 event, suggesting that wastewater disposal may have triggered a low stress drop, otherwise natural earthquake. Additionally, preevent and postevent seismicity in the Raton Basin spatially correlates to regions of subsidence observed in InSAR time series analysis. While these observations cannot discern a causal link between hydrocarbon production and seismicity, they constrain spatial relationships between active basin deformation and geological and anthropogenic features. Furthermore, the InSAR observations highlight the utility of space-based geodetic observations for monitoring and assessing anthropogenically induced and triggered deformation.

### 1. Introduction

The 23 August 2011 Trinidad Colorado earthquake ( $M_w$ 5.3) was the largest instrumentally recorded earthquake along the Rocky Mountain Front Range since the  $M_b$ 5.5 1966 Rocky Mountain Arsenal induced earthquake [Healy *et al.*, 1968; Hsieh and Bredehoeft, 1981] and was widely felt throughout Colorado and northern New Mexico. The U.S. Geological Survey (USGS) National Earthquake Information Center (NEIC) regional W phase centroid moment tensor (CMT) solution for the event indicates normal faulting (strike = 21/185°; dip = 53/38°; and rake = –80/–103°) near the Colorado/New Mexico border in southern Colorado, at a depth of approximately 3 km (<http://www.comcat.cr.usgs.gov>). The event was preceded 4 h by an  $M_w$ 4.7 foreshock and by ~4 months by events of  $M_w$ 3.6 and 3.8 (Figure 1). Immediately following the 2011 Trinidad earthquake, the NEIC deployed four broadband seismometers in the region (Figure 1) to supplement observations from the Advanced National Seismic System (ANSS) backbone network and the Earthscope Transportable Array (TA), with the goal of recording and locating the ensuing aftershock sequence. Twenty-one events recorded during this deployment have subsequently been relocated in order to better constrain aftershock locations and to recalibrate the location of the main shock and foreshocks. Additionally, surface displacements from the earthquake were imaged with spatially dense geodetic observations from interferometric synthetic aperture radar (InSAR), placing constraints on the location and rupture dimensions of the 2011 Trinidad earthquake.

The 2011 earthquake sequence occurred beneath the Raton Basin, a foreland sedimentary basin along the eastern flank of the Rocky Mountains (Figure 1). Here, 2–2.5 km of Cretaceous and Tertiary sedimentary rocks overlie Precambrian crystalline basement that “was intruded” during now-abandoned opening of the Rio Grande rift [Baltz, 1965]. GPS surveys show little surface motion across the Raton Basin, with

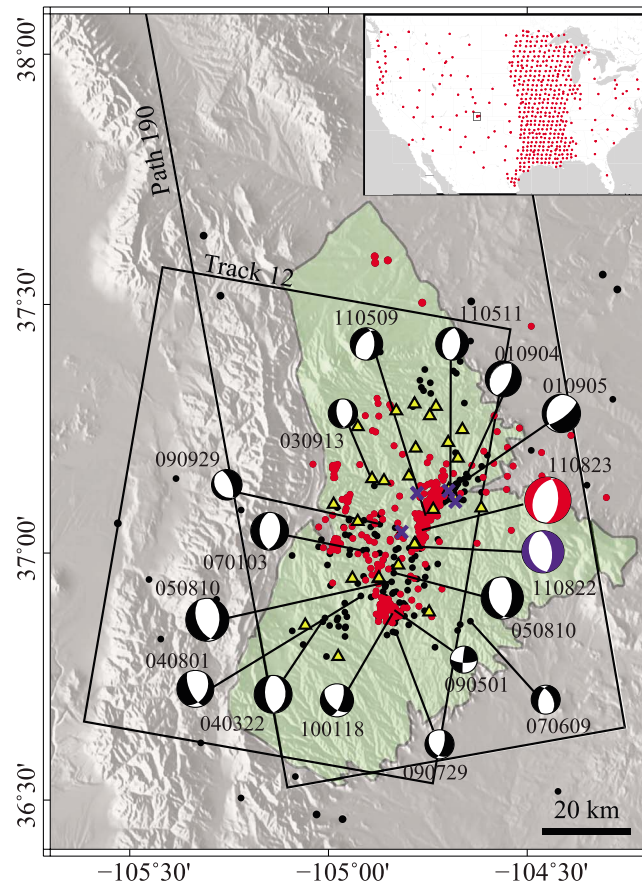


**Figure 1.** Location of the Raton Basin (green outline) and regional seismicity (1966–2013, [Rubinstein et al., 2014]). Regional moment tensor solutions were derived by the NEIC (id = yymmdd, locations match those of Rubinstein et al.). Black dots are seismicity prior to the 2011 Trinidad earthquake (red moment tensor), red dots are seismicity following Rubinstein et al. [2014], blue crosses are the locations of temporary seismometers installed by the USGS following the 2011 Trinidad earthquake. Yellow triangles are wastewater injection wells (www.cogcc.state.co.us). Black-outlined boxes indicate the spatial extent of Envisat (T12) and ALOS (P190) InSAR scenes. Image overlain on shaded Shuttle Radar Topography Mission digital elevation model (SRTM DEM) [Farr et al., 2007]. Red circles in the map inset indicate the locations of all seismometers used to locate the events in Table 1.

<1 mm/yr of east-west extension [Berglund et al., 2012]. Nonetheless, the Raton Basin has hosted many earthquakes over the past half century (Figure 1). Primarily normal faulting in nature, previous notable events occurred in 1966 ( $M_w$ 4.6), 1973 ( $M_w$ 3.1 and 4.2), 2001 ( $M_w$ 4.4), and 2005 ( $M_w$ 5.0) (<http://www.comcat.cr.usgs.gov>).

Like many basins along the Rocky Mountains, the Raton Basin is an active hydrocarbon play for coal bed methane that has been produced since 1999. A percentage of the wastewater produced from the extraction process is disposed in deep wastewater wells (Figure 1) into the Dakota Sandstone, Morrison Formation, and Entrada Sandstone at depths of 1.12–2.2 km, primarily under gravity feed [www.cogcc.state.co.us]. Extraction of coal bed methane occurs at shallower depths from the Raton and Vermejo Formations (www.cogcc.state.co.us). Previous work on earthquakes in the Raton Basin has explored whether there is a link between seismicity and wastewater disposal and extraction processes [Rubinstein et al., 2014; Meremonte et al., 2002; Zhang et al., 2013]. While it is difficult to connect any single earthquake to such processes, the notable increase in seismicity since 2001 and the 2005 and 2011 Trinidad sequences have been attributed to anthropogenic forcing in the basin [Rubinstein et al., 2014; Ellsworth, 2013].

In this work, we provide seismological and InSAR constraints on basinwide deformation over the period of 2007–2012 and on the spatial kinematics of the 2011 Trinidad earthquake and aftershock sequence. We show that the 2011 earthquake ruptured the underlying crystalline basement of the Raton Basin and that the two May 2011 earthquakes likely occurred on the same structure. We also explore InSAR time series analysis and show that resolvable subsidence in the basin is spatially correlated to increased seismicity [Rubinstein et al., 2014] that occurred prior to and following the Trinidad earthquake.

## 2. Methods

### 2.1. Foreshock, Main Shock, and Aftershock Locations

Following the 2011  $M_w$ 5.3 Trinidad earthquake, the USGS NEIC located 584 aftershocks over the time period 23 August 2011 to 15 December 2011 within the Raton Basin (Figure 2a). These events were located using the ANSS backbone network, the Earthscope TA, and four broadband seismometers (Figure 1) installed on 23 August in the vicinity of the Trinidad main shock and recorded throughout the period of

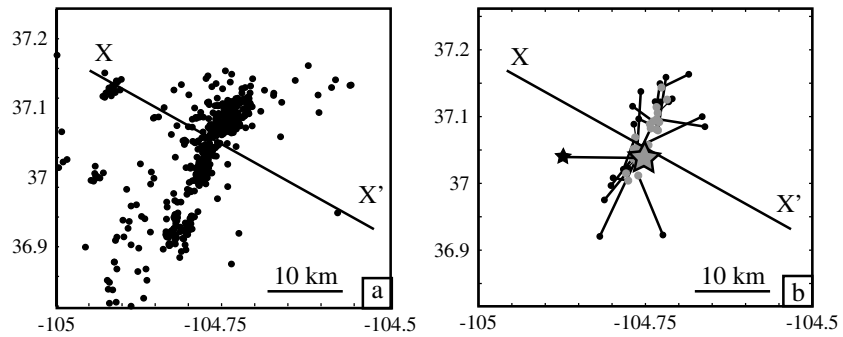


**Figure 2.** Seismicity of the 2011 Trinidad sequence (May 2011 to December 2011). (a) Preliminary earthquake locations from the NEIC. (b) Twenty-one relocated events using HDC (see text for details). Black dots indicate the original locations, gray dots the relocations, joined by relocation vectors. Star: 2011 Trinidad main shock.

analysis. The 584 earthquakes were initially located using standard NEIC single-event procedures that use the AK135 global velocity model [Kennett *et al.*, 1995]. Each arrival time pick was manually reviewed prior to locating. A local magnitude ( $M_L$ ) was computed for all of the events in the study.

After initial locations were determined, 21 events were relocated using hypocentroidal decomposition (HDC) [Jordan and Sverdrup, 1981] as implemented and described in other studies [McNamara *et al.*, 2014; Hayes *et al.*, 2013] (Figure 2b and Table 1). Through this methodology, the earthquake location problem is divided into two parts—the relative location between events within a cluster and the absolute location of the cluster itself. The relocated sequence was divided into two clusters. The first cluster includes 2 days of aftershocks following the Trinidad earthquake with events observed by both regional and temporary

**Table 1.** Relocated Earthquakes<sup>a</sup>

Date <sup>b</sup>	OT1	Lon1	Lat1	OT2	Lon2	Lat2	Z (km)
2011/5/9	28:52.8	-104.783	37.021	28:51.2	-104.76534	37.06877	3 <sup>d</sup>
2011/5/11	06:15.3	-104.665	37.1	06:13.2	-104.76775	37.05136	3 <sup>d</sup>
2011/8/22	30:18.1	-104.8114	36.9751	30:17.1	-104.77892	37.05834	3 <sup>d</sup>
2011/8/23	48:50.3	-104.7238	36.9226	48:48.7	-104.76071	37.01174	3 <sup>d</sup>
2011/8/23 <sup>c</sup>	46:17.8	-104.8722	37.0394	46:15.4	-104.75298	37.03811	3 <sup>d</sup>
2011/8/23	12:18.3	-104.715	37.1222	12:58.6	-104.71761	37.12538	3 <sup>d</sup>
2011/8/23	56:57.6	-104.6608	37.0849	56:55.9	-104.73306	37.09641	3 <sup>d</sup>
2011/8/23	01:33.5	-104.7282	37.1493	01:31.9	-104.73334	37.11427	3 <sup>d</sup>
2011/8/23	17:59.1	-104.7098	37.1266	17:56.2	-104.73158	37.10547	3 <sup>d</sup>
2011/8/23	34:39.7	-104.7693	37.1155	34:37.3	-104.73845	37.09292	3 <sup>d</sup>
2011/8/23	32:17.1	-104.6852	37.1633	32:15.7	-104.72594	37.14349	3 <sup>d</sup>
2011/8/23	37:57.1	-104.7984	37.0082	37:54.4	-104.77573	37.00424	3 <sup>d</sup>
2011/8/23	29:27.9	-104.8184	36.9205	29:29.6	-104.74202	37.08241	3 <sup>d</sup>
2011/8/23	03:50.4	-104.7569	37.1376	03:17.9	-104.76328	37.03284	3 <sup>d</sup>
2011/8/23	11:12.9	-104.8015	36.9967	11:10.6	-104.76907	37.03746	3 <sup>d</sup>
2011/8/24	40:43.2	-104.7672	37.0886	40:42.5	-104.76219	37.05419	5.95
2011/8/24	07:49.4	-104.7354	37.1224	07:48.8	-104.7338	37.08096	5.31
2011/8/24	15:52.6	-104.7192	37.1589	15:51.7	-104.73122	37.0794	4.42
2011/8/24	39:48.4	-104.7278	37.122	39:47.1	-104.72931	37.09176	5.72
2011/8/25	44:35.8	-104.7601	37.0966	44:35.6	-104.74323	37.08858	4.94
2011/8/25	34:33.8	-104.7764	37.0235	34:34.1	-104.74538	37.05739	5.65

<sup>a</sup>OT1, Lon1, and Lat1 indicate origin time, longitude, and latitude from the NEIC/Hydra location. OT2, Lon2, and Lat2 indicate origin time, longitude, and latitude of the relocated event.

<sup>b</sup>Dates are formatted as yy/mm/dd.

<sup>c</sup>The 2011 Trinidad earthquake main shock.

<sup>d</sup>Fixed values of depth. Relative position between locations for each event are shown in Figure 3b. All depths are relative to mean sea level. The surface elevation in the Raton Basin near the 2011 Trinidad epicenter is ~2.1 km above sea level.

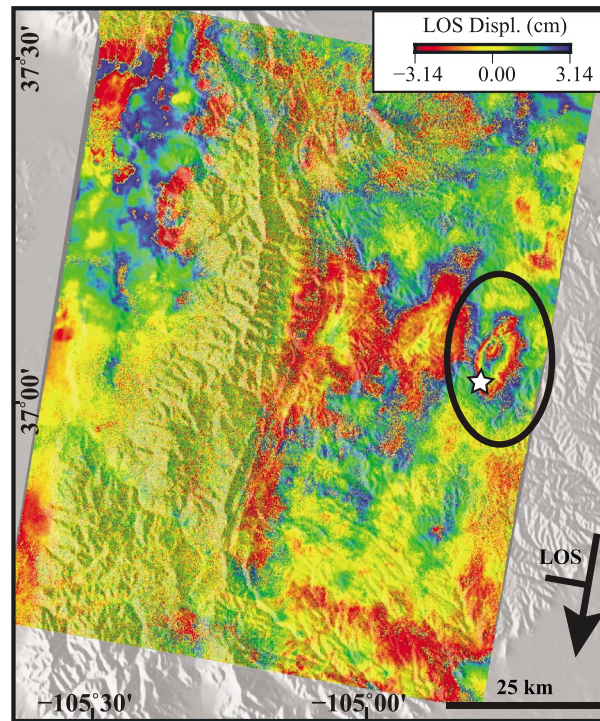


**Figure 3.** Envisat wrapped descending interferogram (26 April 2011 to 23 September 2011, Table 2) showing surface displacements caused by the 2011 Trinidad earthquake. Our relocated hypocenter (Table 1) is shown with a star. LOS (line of sight) and arrow indicate the travel and look direction of the satellite. All coseismic interferograms are detailed in Table 2. Image overlain on Shuttle Radar Topography Mission (SRTM) digital elevation model (DEM) [Farr et al., 2007]. Inset shows the spatial extent of the interferogram. Resampled interferograms are shown in Figure S1.

seismic stations. The locations of earthquakes in this cluster were then used to calibrate locations of events in the second cluster that was regionally recorded prior to installation of the portable stations. This second cluster includes the main shock, foreshocks, and two  $M4+$  events in May 2011. Both clusters were relocated relative to each other using observations from common regional stations in order to connect the clusters in an absolute framework. During this process, greater weight was placed on those events located with the temporary local stations, which can be considered as calibrated absolute locations. All events were located using manual  $P$  wave picks only, and depth was fixed to 3 km (depth below mean sea level) for events in the first cluster (those that occurred before the temporary array was installed) (Table 1). Epicentral location uncertainties were also estimated for the 21 relocated events. Implementation of HDC on the aftershock sequence results in the collapse of a diffuse cloud of sources onto a well-defined linear trend aligned approximately northeast-southwest (Figure 2b). The Trinidad main shock moved 10.6 km from an initial location of  $104.872^\circ\text{W } 37.0394^\circ\text{N}$  to  $104.75298^\circ\text{W } 37.03811^\circ\text{N}$ . The HDC

processing resulted in an average epicentral shift of  $9.4 \pm 2.2$  km for the main shock and pre-main-shock earthquakes, whereas the epicentral shift in the aftershock locations was  $5.5 \pm 4.5$  km. These locations are in agreement, within uncertainties, with events in the catalog of Rubinstein et al. [2014].

### 2.2. InSAR Analysis: 2011 Trinidad Earthquake

InSAR observations of ground displacements from shallow earthquakes complement seismic studies in many cases, affording constraints on the finite dimensions and locations of slip as well as providing a more precise indication of the earthquake centroid. These constraints in turn allow us to explore relationships between distributed finite slip, earthquake point source locations, local geology, and anthropogenic activity. To further constrain the source characteristics of the  $M_w 5.3$  2011 Trinidad earthquake, we analyze four

**Table 2.** InSAR Observations Used in This Study to Constrain the 2011 Trinidad Coseismic Slip<sup>a</sup>

Satellite	Track	Date 1	Date 2	$B_{\text{perp}}$ (m)
ENVI	12	2011/4/26	2011/9/23	208.5
ENVI	12	2011/4/26	2011/11/22	444
ENVI	12	2011/4/26	2012/1/21	124.5
ENVI	12	2011/5/26	2011/9/23	421

<sup>a</sup>Satellite indicates source instrument (ENVI = Envisat); Track is observational ID; Date 1 and Date 2 indicate preseismic and postseismic acquisitions, formatted as yy/mm/dd;  $B_{\text{perp}}$  is the perpendicular baseline, in meters, between acquisitions.

descending interferograms processed from the Envisat C band SAR (Figure 3, Table 2, and Figure S1 in the supporting information). Interferograms were processed with the Caltech/JPL ROI-PAC processing software [Rosen et al., 2004], and topographic phase was removed with the 90 m Shuttle Radar Topography Mission (SRTM) digital elevation model (DEM) [Farr et al., 2007]. Individual scenes

were unwrapped with the branch cut region growing algorithm [Goldstein *et al.*, 1988]. Each scene is then downsampled to a computationally feasible  $\sim 10^4$  pixels, and an estimate of covariance structure is derived (Figure S1) [Lohman and Simons, 2005; Lohman and Barnhart, 2010]. We also search Envisat and ERS images for surface displacements from the 2001 ( $M_w 4.4$ ) Trinidad and 2005 New Mexico ( $M_w 5.0$ ) earthquakes (Figure 1) [Meremonte *et al.*, 2002]; however, radar decorrelation prevented us from unambiguously identifying signals from these events.

A significant limitation of this InSAR data set is the availability of only one look direction and a lack of additional constraints on coseismic surface displacements, such as GPS. The single look direction, the blind nature of the event, and the small magnitude of surface displacements compared to noise in the data potentially lead to an unstable inverse problem where fault plane geometry and dimensions may trade off significantly when attempting to invert for distributed slip [e.g., Devlin *et al.*, 2012; Scott *et al.*, 2014]. To address these issues, we generate three candidate slip distributions following the general methodology of Barnhart *et al.* [2013, 2014], beginning with inverting for fault geometry and location. We have explicitly chosen to focus on the east dipping focal plane, as this is consistent with both the depth distribution of aftershocks [Rubinstein *et al.*, 2014] and previous events in this region [Meremonte *et al.*, 2002]. For each model, we first invert the downsampled interferograms for the geometry (strike, dip, rake, length, and width) and location (longitude, latitude, and depth) of a single rectangular fault patch with uniform slip embedded in a homogeneous elastic half space [Okada, 1992] using the Neighbourhood Algorithm [Sambridge, 1999]. To generate the first model geometry (Model 1), we invert the surface displacements allowing for a broad range of model parameters (strike = 10 to 40, dip = 20 to 80, rake =  $-120$  to  $-60$ , length = 7 to 12 km, and width = 4 to 7 km), and we add no additional constraint from moment tensors or focal mechanisms. We choose the best model based on that which minimizes the misfit to the observed data. As there is no spatial smoothing in an inversion for slip on a single fault patch, we need not consider the relative contributions of oversmoothing and under-smoothing the model.

The second model geometry (Model 2) is derived through an approach designed to address potential tradeoffs between strike/dip/rake and fault dimensions. We conduct 1000 inversions wherein we randomly combine fixed values of strike, dip, and rake (over the range described above), and invert for fault length, width, and location using the Neighbourhood Algorithm (Figure S2). As before, we then choose the best model based on the combination of geometric descriptors that produce the lowest model residual. Lastly, the third model geometry (Model 3) is strictly constrained by the W phase regional moment tensor. We fix strike ( $21^\circ$ ) and dip ( $54^\circ$ ), then invert for rake, length, width, and location with the Neighbourhood Algorithm.

After we have inverted for fault geometry and location using these three approaches, we fix the planes in space and extend them both along strike and down dip to eliminate artifacts in inverted slip caused by the model edges. We then invert for distributed slip (Figure 4) using an iterative algorithm that generates a variably discretized fault plane wherein the sizes of individual subfaults reflect the model resolution [Barnhart and Lohman, 2010]. We fix rake to the best fit rake from the Neighbourhood Algorithm, and we impose length scale independent minimum moment regularization. Our preferred models are chosen using the  $R_i$  criterion, which chooses a “best” model based on the slip distribution that fits the underlying, error free tectonic signal while minimizing the mapping of data noise and regularization errors [Barnhart and Lohman, 2010]. We likewise assess the contributions of correlated atmospheric noise on the presented slip distributions [Barnhart and Lohman, 2013b]. We add 500 realizations of synthetic noise to the displacements predicted by the best fit slip distributions, then invert each synthetic data set onto the discretized fault planes using the same regularization [Barnhart and Lohman, 2013b]. This Monte Carlo analysis only constrains uncertainties in slip due to atmospheric noise and our choice of smoothing and does not account for the effects of unwrapping errors, incorrect model geometry, or inferred rigidity structure. Figure S3 shows the 1 sigma bounds of slip, which are defined as the sixteenth and 84th percentiles due to the non-Gaussian distribution.

### 2.3. InSAR Time Series

In addition to deformation resulting from the 2011 Trinidad main shock, we search for preseismic and postseismic ground displacements, whether tectonic or anthropogenic, in the Raton Basin (Figure 5). In order to constrain preseismic ground displacements, we construct a  $\sim 4$  year InSAR time series using images from the Japanese Space Agency ALOS L band instrument. We use 17 acquisitions, from 21 July 2007 to

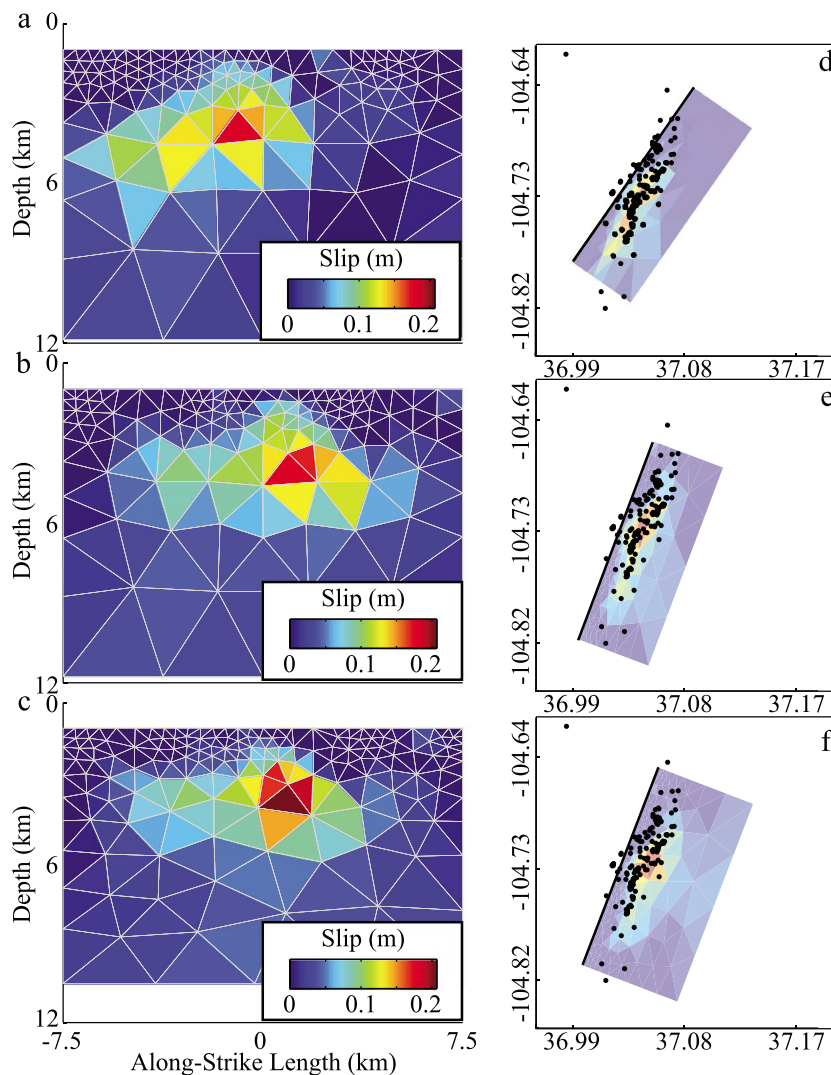


**Figure 4.** Slip distributions derived for the 2011 Trinidad earthquake. (a–c) Strike normal view of slip distributions derived for Models 1–3 (Table 3), each plotted with same color and depth (0–12 km) ranges. (d–f) Map view image of each slip distribution with preliminary aftershocks locations located by the NEIC. Heavy black line indicates the top of each southeast dipping fault plane. Slip distribution uncertainty results are shown in Figure S3.

16 March 2011, and construct all interferograms with spatial baselines of <1000 m (Figure S4). For the postseismic period, we use six Envisat acquisitions over six months (23 September 2011 to 21 March 2012) to generate interferograms that are inspected individually for postseismic deformation. Interferograms are processed using the methodology described above. All unwrapped interferograms within each pre/postseismic time interval are coregistered to a single master scene in the radar coordinate reference frame. We then remove a quadratic function from each scene to account for signal induced by satellite orbital position errors, and we invert for the time displacement history of each spatially unwrapped pixel [Berardino *et al.*, 2002; Barnhart and Lohman, 2012]. Reported surface velocities are generated from a linear fit to the inverted time displacement histories of each pixel.

### 3. Results

#### 3.1. InSAR: Coseismic Rupture

The results of our fault geometry/location and slip distribution inversions are shown in Table 3 and Figure 4. The slip distributions demonstrate broadly similar characteristics, with an along-strike rupture length of 8

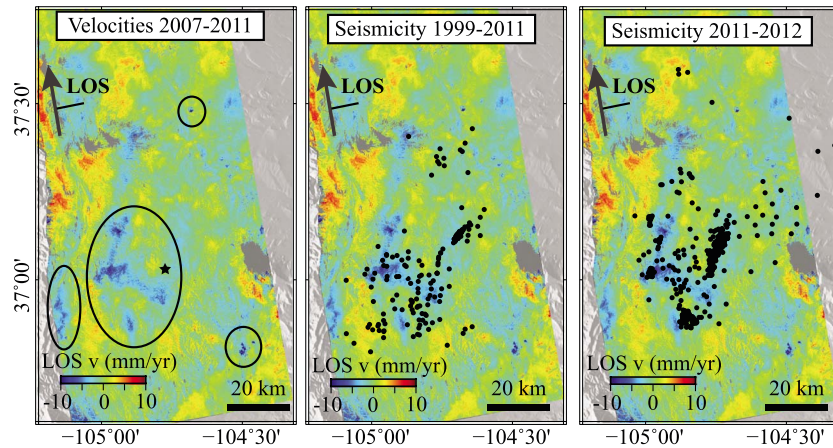


**Figure 5.** Line-of-sight (LOS) surface velocities inferred from preseismic ALOS time series (2007–2011). Positive is motion toward the satellite, negative is motion away from the satellite (e.g., subsidence). (a) Annotated time series indicating regions of resolvable subsidence (circled) and the epicentral location of the 2011 Trinidad earthquake (star). (b) Pre-Trinidad earthquake seismicity (1999 to 22 August 2011) [Rubinstein et al., 2014] overlain on LOS velocities. (c) Post-Trinidad earthquake seismicity (23 August 2011 to 10 December 2013) overlain on LOS velocities. Imagery dates and interferometric pairs used are detailed in Figure S4. Images are overlain on SRTM DEM [Farr et al., 2007], LOS, and arrows indicate the satellite motion and look directions.

to 10 km, depth range of 1.4 to 6.3 km, a centroid depth (defined as the center of the patch with maximum slip) of 3.7 to 4.1 km, and nearly identical  $\beta_r$  values. The slip distribution for Model 1 (Figure 4a), which is rotated substantially from the W phase regional CMT, exhibits slip to 8.6 km; however, this deeper slip may result from smoothing or incorrect model geometry. Furthermore, our procedure of iterating over 1000 possible model combinations shows that there are clear minima of strike and dip that correspond to the lowest model residual, whereas length and width do not exhibit a clear minimum correlated to the best fitting strike and dip (Figure S2). This indicates that the InSAR observations constrain the fault orientation well, but length and width trade off substantially and inhibit a proper fit to the strike and dip when allowed to vary. These inversion results and the consistency of Models 2 and 3 with the orientation of the regional W phase CMT lead us to conclude that Models 2 and 3 provide the more realistic images of slip during this event. At the same time, the difference in strike between Models 1 and 2/3 (Table 3 and Figures 4d–4f) may reflect along-strike curvature of the structure or multiple fault planes, neither of which we attempt to constrain in our modeling. Our results highlight the potential dangers in assuming that a single “best fit” faulting solution provides the most reasonable geological interpretation in scenarios where additional information (e.g., CMTs, aftershock locations) is not available. Nonetheless, these results also inhibit our ability to confidently interpret details of the slip distributions; thus, we only interpret the broad-scale features of the slip distributions that are consistent between models (e.g., length, depth, and centroid location).

The depth of imaged slip shows that the 2011 Trinidad earthquake ruptured the crystalline basement (>2 km depth) underlying the sedimentary section of the Raton Basin. As noted by Rubinstein et al. [2014], the 2011 Trinidad earthquake, and subsequent or prior seismicity, is likely not related to minor normal faults mapped throughout the Raton Basin. In all three of the slip distributions, the relocated hypocenter for

**Table 3.** Fault Model Parameters for the Three Fault Geometries Tested (Figure 4)<sup>a</sup>

Model	Lon0	Lat0	LonC	LatC	Zc (km)	Strike	Dip	Rake	Mw
1	−104.80	37.03	−104.75	37.08	4.05	35	65	−66	5.47
2	−104.79	37.01	−104.75	37.07	4.15	22	64	−76	5.41
3	−104.79	37.01	−104.74	37.08	3.75	21	53	−89	5.49

<sup>a</sup>Lon0/Lat0 indicate the southern vertex of the top of the fault plane; LonC/LatC/Zc indicate the location and depth of the imaged centroid (center of the fault patch with the greatest slip); Strike/Dip/Rake are values inferred from the Neighbourhood Algorithm or the tests shown in Figure S2. Mw is the inverted moment magnitude of slip distributions shown in Figure 4.

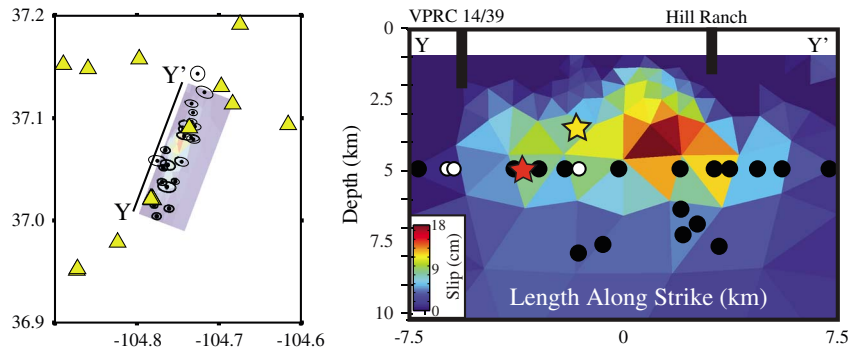


**Figure 6.** (a) Aftershocks relocated with HDC and inferred epicentral error ellipses overlain on the Model 2 slip distribution (Figure 4b). Profile Y-Y' is the surface projection of the fault plane. Yellow triangles are locations of wastewater disposal wells. (b) Strike normal view of slip distribution (Figure 4b) along profile Y-Y' (Figure 6a). Black dots are aftershocks located with HDC (Figure 6a), and white dots are preshocks located with HDC. Red star: hypocenter relocated through HDC. Yellow star: hypocenter from Rubinstein et al. [2014]. Vertical bars show the injection depths and locations of wastewater disposal wells. All HDC hypocenters are adjusted 2.1 km deeper to account for their location relative to mean sea level.

the  $M_w$ 5.3 event [Rubinstein et al., 2014, this study] is located near the southern terminus of the mapped slip. This indicates that the rupture propagated 8–10 km toward the north, with the primary moment release (centroid) occurring north of the rupture initiation. Additionally, the length of rupture imaged geodetically

is longer than expected for an  $M_w$ 5.3 blind intraplate normal faulting earthquake [Wells and Coppersmith, 1994]. An earthquake of, conservatively,  $M_w$ 5.8 ( $\pm 0.38$ ) would be expected to produce an earthquake of the imaged length (8–10 km) [Wells and Coppersmith, 1994].

### 3.2. Earthquake Catalog

Initial aftershock locations determined by the USGS define a broad cloud of seismicity in the vicinity of the inferred coseismic fault plane (Figures 2a and 4d–4f). Relocations exhibit error ellipses that are oriented approximately perpendicular to the inferred Trinidad main shock fault plane, such that all relocated events—including foreshocks, main shock, aftershocks, and the May 2011 events—fall on the inferred fault plane within uncertainties (Figure 6a). This suggests that all events likely occurred on the same fault plane or in the immediate vicinity of the same fault plane along parallel structures.

The USGS aftershock catalog from 23 August 2011 to 15 December 2011 is complete to approximately  $M_L$ 1.0 (Figure 7, top). The  $b$  value of this Gutenberg-Richter magnitude frequency distribution is 0.65. A higher magnitude of completeness of  $M_L$ 1.5 raises the  $b$  value only marginally to 0.67. Although low with respect to global averages and to the magnitude frequency distributions of normal faulting events, these  $b$  values are consistent with other earthquake sequences, both natural and induced, within cratonic North America [Frohlich and Davis, 1993]. For comparison, the 2011 Mineral,

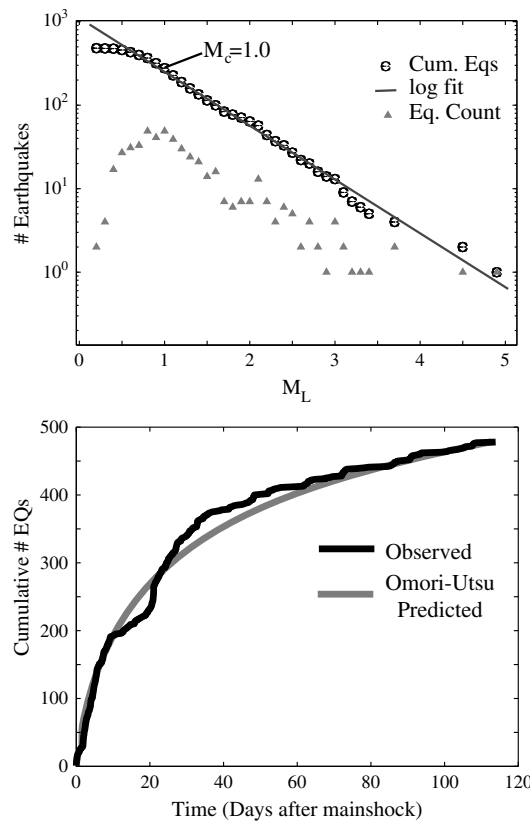


**Figure 7.** (top)  $B$  value and (bottom) Omori's Law plots for 584 aftershocks located by the NEIC. Earthquake magnitudes are  $M_L$ . The  $B$  value is 0.65, assuming the magnitude of completeness ( $M_c$ ) is 1.0. The Omori-Utsu relationship values for the predicted curve (Figure 7, bottom) is  $p = 1.14$ ,  $c = 5$ , and  $k = 235.4$ .

Virginia and Prague, Oklahoma earthquakes, which are inferred to be natural and induced earthquakes respectively, exhibit  $b$  values of 0.75 and 0.62 [Ellsworth, 2013; Keranen *et al.*, 2013; McNamara *et al.*, 2014]. Additionally, the 2011 Trinidad aftershock sequence decays at a fast rate consistent with other intraplate earthquakes [Guo and Ogata, 1997], exhibiting an Omori-Utsu  $p$  value of 1.14 (Figure 7, bottom). Additionally, the regional W phase CMT (<http://www.comcat.cr.usgs.gov>) exhibits only a 5% nondouble couple component, indicating little to no volumetric strain occurred. These three observations alone indicate that the Trinidad main shock rupture and aftershock sequence reflect characteristics common in natural earthquakes. Approximately 74–78% of the aftershocks located by Rubinstein *et al.* [2014] occurring from 23 August 2011 to 23 September 2011 on the main shock fault plane (defined as events that form a lineament parallel to the InSAR-inferred fault plane) occur within the spatial length of rupture, with the majority of events collocated with deeper slip. Remaining on-fault aftershocks are located to the north along strike, consistent with increased stress from directed northward slip propagation.

### 3.3. InSAR Time Series

The InSAR time series analysis reveals a combination of topographic/atmospheric artifacts and resolvable surface subsidence (Figure 5). To discern between tropospheric-induced path delays that propagate through the temporally sparse time series and real ground displacements, we first ignore any velocities from  $-5$  to  $5$  mm/yr, which are conservatively below the detection threshold of real ground displacements for this time series [Barnhart and Lohman, 2013a]. Second, we assess both the spatial correlation between velocities and topography and the temporal persistence of uplift/subsidence signals (Figure S5). By these criteria, we find that the primary uplift signals (positive velocities) are likely tropospheric noise as these signals correlate spatially to steep topography along the western margin of the Raton Basin. We also find no resolvable uplift or subsidence in the rupture region of either the 2005 or 2011 earthquake sequences. Last, we find no uplift signals that correlate spatially to wastewater injection wells. This is not unexpected given the depth range of injection.

Conversely, we find regions of subsidence, in some cases exceeding  $10$  mm/yr, that likely reflect real ground displacements as they do not correlate to topography (Figure S5) and are persistent over the 4 year time series. These regions of preseismic subsidence, which we infer result from shallow fluid (methane and/or ground water) withdrawal, exhibit a strong spatial correlation to both pre- and post-2011 event seismicity across Raton Basin [Rubinstein *et al.*, 2014]. This subsidence is inconsistent with a magmatic source (e.g., dyke intrusion) because the spatial wavelengths of deformation require very shallow ( $<10$  km) magmatic sources that would create a thermal state incompatible with the existence of coal bed methane. Furthermore, these signals are not consistent with the easily diagnosed magmatic signals commonly observed in other regions.

Prior to the 2011 Trinidad earthquake, seismicity in the basin is broadly distributed in the regions of subsidence centered near  $37^{\circ}\text{N}$ , with the exceptions of the 2011 foreshock sequence and the 2005 earthquake sequence (Figure 5b). Following the August 2011 earthquake, many events occur in this broadly subsiding region as well (Figure 5c). Notably, two clusters of earthquakes appear beyond the aftershock sequence—one centered on a well-defined region of preseismic subsidence and one offset to the east from another region of preseismic subsidence and west of the 2005 New Mexico earthquake sequence.

Postseismic interferograms following the 2011 Trinidad earthquake reveal no detectable signal of postseismic processes, such as pore fluid flow or afterslip.

## 4. Conclusions

The work presented here highlights spatial constraints on a potentially induced or triggered earthquake and the role of geodesy in future studies of induced seismicity, though they cannot make a direct causal link between anthropogenic processes and seismicity. The August 2011  $M_w$ 5.3 Trinidad earthquake ruptured a southeast dipping normal fault with a similar mechanism to the 2001 Trinidad earthquake [Meremonte *et al.*, 2002]. Two events in May 2011, as well as foreshocks on 22 and 23 August 2011, all likely occurred on the same fault plane as the August main shock. InSAR constraints on finite fault slip entail variability in the details of source characteristics depending on inferred geometry; however, consistent characteristics show slip propagated unilaterally to the north and ruptured within the crystalline Precambrian basement at depths of  $1.4$ – $6$  km. Well-resolved slip propagates to shallower depths of  $1.5$  km, and this could reflect either slip in the sedimentary section or local basement relief. The aftershock sequence of the Trinidad

earthquake exhibits statistical properties ( $b$  value, Omori-Utsu decay constant) expected for intraplate earthquakes, and the  $W$  phase CMT of the main shock exhibits little to no volumetric strain which might be expected for an induced earthquake. However, these observations carry the important caveat that the earthquake itself exhibited unusually long length characteristics that may suggest a low stress drop event. This low stress drop inference is further evidenced by an apparent stress (0.07 MPa, <http://www.comcat.cr.usgs.gov>) that is much lower than expected for intraplate normal faulting events [Choy and Boatwright, 1995; Boatwright et al., 2002]. Furthermore, the earthquake nucleated in the vicinity of and  $\sim 3$  km beneath a cluster of wastewater disposal sites (VPRC 14/39) that have been active since 1999 (Figure 6). The rupture propagated toward another injection well, Hill Ranch, which has been active over the same period. If there is a link between this earthquake and those wastewater disposal wells, the 2011 earthquake likely reflects rupture of a naturally stressed fault with the initiating stresses provided by wastewater disposal at sites VPRC 14/39. This hypothesis would dictate that the Trinidad earthquake was triggered by wastewater injection. In this scenario, the spatial and temporal separation between wastewater disposal and rupture within the basement would thus be explained by propagation of hydrological stresses from basin bottom sedimentary units into the faulted crystalline basement [Zhang et al., 2013; Keranen et al., 2014]. The juxtaposition of characteristics common for natural intraplate earthquakes with the potential low stress drop of the event and regional context of wastewater disposal indicate that, if the 2011 Trinidad earthquake was triggered, anthropogenic processes may affect the timing and location of otherwise natural seismicity.

Additionally, InSAR time series analysis potentially reveals the source of a separate class of seismicity in the Raton Basin induced by fluid withdrawal. Our time series analysis shows active localized subsidence over the observation period (2007–2011) throughout the basin. These subsiding regions likely result from the withdrawal of coal bed methane, as observed in other regions such as Iran [Barnhart and Lohman, 2012] and/or ground water, and the deformation and presence of producible methane are inconsistent with the existence of magmatic sources. The spatial correlation between subsidence and regions of increased seismicity both before and after the 2011 Trinidad earthquake suggests that there may be a physical link between fluid withdrawal and enhanced seismicity in these regions, both with respect to ongoing increased seismicity (2001–present) and triggered seismicity following the 2011 Trinidad earthquake. The magnitudes of earthquakes in the Raton Basin are likewise too small to produce a subsidence signal of the magnitude and length scale observed. However, given the high noise levels in the time series, short temporal observation period, and the lack of precise depths for many of these earthquakes, we can only identify the spatial relationships between these independent observations.

Our observations of the 2011 Trinidad earthquake rupture, seismicity, and ongoing subsidence in Raton Basin demonstrate spatial links between seismicity and both wastewater disposal practices and fluid withdrawal. In turn, these observations may help to elucidate physical forcing, or lack thereof, between earthquakes and anthropogenic activity in the Raton Basin and elsewhere. As noted by other authors, increased seismicity rates in Raton Basin that correlate temporally to increased volumes of wastewater disposal reflect anthropogenic forcing [Rubinstein et al., 2014; Ellsworth, 2013]. However, in order to fully relate seismicity, anthropogenic processes, and observable ground deformation, which in turn provide information on the mechanical and hydrological kinematics contributing to basin deformation, higher-precision observations, both spatially and temporally, are necessary. These include precise earthquake locations from dense regional seismic networks, detailed information on subsurface geology and hydrology, continuous records of fluid extraction and wastewater disposal, and systematic monitoring of temporal and spatial changes of ground deformation from InSAR. Forthcoming InSAR missions, including ALOS-2 and NISAR, as well as the now launched Sentinel-1, have the potential to provide spatially and temporally dense monitoring of induced deformation globally. Convolving observations of ongoing ground deformation with seismicity and hydrological modeling [Keranen et al., 2014] will help to provide a physical framework for induced seismicity and assist in mitigating the social risk arising from seismicity in previously quiescent regions.

#### Acknowledgments

The authors thank the Associate Editor, Chuck Wicks, and two anonymous reviewers for comments that substantially improved this manuscript. Envisat SAR images were acquired through the UNAVCO WInSAR data portal; ALOS images were acquired through the Alaska Satellite Facility via a research user agreement. This work was supported in part by the USGS Mendenhall postdoctoral program and USGS Geological Hazards program. Several figures were generated using the Generic Mapping Tool [Wessel and Smith, 1998]. Any use of trade, product, or firm names is for descriptive purposes only and does not imply endorsement by the U.S. government.

#### References

- Baltz, E. H. (1965), Stratigraphy and history of Raton Basin and notes on San Luis Basin, Colorado-New Mexico, *AAPG Bull.*, 49(11), 2041–2075.
- Barnhart, W. D., and R. B. Lohman (2010), Automated fault model discretization for inversions for coseismic slip distributions, *J. Geophys. Res.*, 115, B10419, doi:10.1029/2010JB007545.
- Barnhart, W. D., and R. B. Lohman (2012), Regional trends in active diapirism revealed by mountain range-scale InSAR time series, *Geophys. Res. Lett.*, 39, L08309, doi:10.1029/2012GL051255.

- Barnhart, W. D., and R. B. Lohman (2013a), Characterizing and estimating noise in InSAR and InSAR time series with MODIS, *Geochem. Geophys. Geosyst.*, *14*, 4121–4132, doi:10.1002/ggge.20258.
- Barnhart, W. D., and R. B. Lohman (2013b), Phantom earthquakes and triggered aseismic creep: Vertical partitioning of strain during earthquake sequences in Iran, *Geophys. Res. Lett.*, *40*, 819–823, doi:10.1002/grl.50201.
- Barnhart, W. D., R. B. Lohman, and R. J. Mellors (2013), Active accommodation of plate convergence in Southern Iran: Earthquake locations, triggered aseismic slip, and regional strain rates, *J. Geophys. Res. Solid Earth*, *118*, 5699–5711, doi:10.1002/jgrb.50380.
- Barnhart, W. D., G. P. Hayes, S. V. Samsonov, E. J. Fielding, and L. E. Seidman (2014), Breaking the oceanic lithosphere of a subducting slab: The 2013 Khash, Iran earthquake, *Geophys. Res. Lett.*, *41*, 32–36, doi:10.1002/2013GL058096.
- Berardino, P., G. Fornaro, R. Lanari, and E. Sansosti (2002), A new algorithm for surface deformation monitoring based on small baseline differential SAR interferograms, *IEEE Trans. Geosci. Remote Sens.*, *40*(11), 2375–2383, doi:10.1109/TGRS.2002.803792.
- Berglund, H. T., A. F. Sheehan, M. H. Murray, M. Roy, A. R. Lowry, R. S. Nerem, and F. Blume (2012), Distributed deformation across the Rio Grande Rift, Great Plains, and Colorado Plateau, *Geology*, *40*(1), 23–26, doi:10.1130/G32418.1.
- Boatwright, J., G. L. Choy, and L. C. Seekins (2002), Regional estimates of radiated seismic energy, *Bull. Seismol. Soc. Am.*, *92*(4), 1241–1255, doi:10.1785/0120000932.
- Choy, G. L., and J. L. Boatwright (1995), Global patterns of radiated seismic energy and apparent stress, *J. Geophys. Res.*, *100*(B9), 18,205–18,228, doi:10.1029/95JB01969.
- Devlin, S., B. L. Isacks, M. E. Pritchard, W. D. Barnhart, and R. B. Lohman (2012), Depths and focal mechanisms of crustal earthquakes in the central Andes determined from teleseismic waveform analysis and InSAR, *Tectonics*, *31*, TC2002, doi:10.1029/2011TC002914.
- Ellsworth, W. L. (2013), Injection-induced earthquakes, *Science*, *341*(6142), doi:10.1126/science.1225942.
- Farr, T. G., et al. (2007), The shuttle radar topography mission, *Rev. Geophys.*, *45*, RG2004, doi:10.1029/2005RG000183.
- Frohlich, C., and S. D. Davis (1993), Teleseismic *b* values; Or, much ado about 1.0, *J. Geophys. Res.*, *98*(B1), 631–644, doi:10.1029/92JB01891.
- Goldstein, R. M., H. A. Zebker, and C. L. Werner (1988), Satellite radar interferometry: Two-dimensional phase unwrapping, *Radio Sci.*, *23*(4), 713–720, doi:10.1029/RS023i004p00713.
- Guo, Z., and Y. Ogata (1997), Statistical relations between the parameters of aftershocks in time, space, and magnitude, *J. Geophys. Res.*, *102*(B2), 2857–2873, doi:10.1029/96JB02946.
- Hayes, G. P., E. Bergman, K. L. Johnson, H. M. Benz, L. Brown, and A. S. Meltzer (2013), Seismotectonic framework of the 2010 February 27 *Mw* 8.8 Maule, Chile earthquake sequence, *Geophys. J. Int.*, *195*(2), 1034–1051, doi:10.1093/gji/ggt238.
- Healy, J. H., W. W. Rubey, D. T. Griggs, and C. B. Raleigh (1968), The Denver earthquakes, *Science*, *161*(3848), 1301–1310, doi:10.1126/science.161.3848.1301.
- Hsieh, P. A., and J. D. Bredehoeft (1981), A reservoir analysis of the Denver earthquakes: A case of induced seismicity, *J. Geophys. Res.*, *86*(B2), 903–920, doi:10.1029/JB086iB02p00903.
- Jordan, T. H., and K. A. Sverdrup (1981), Teleseismic location techniques and their application to earthquake clusters in the South-Central Pacific, *Bull. Seismol. Soc. Am.*, *71*(4), 1105–1130.
- Kennett, B. L. N., E. R. Engdahl, and R. Buland (1995), Constraints on seismic velocities in the Earth from traveltimes, *Geophys. J. Int.*, *122*(1), 108–124, doi:10.1111/j.1365-246X.1995.tb03540.x.
- Keranan, K. M., H. M. Savage, G. A. Abers, and E. S. Cochran (2013), Potentially induced earthquakes in Oklahoma, USA: Links between wastewater injection and the 2011 *Mw* 5.7 earthquake sequence, *Geology*, doi:10.1130/G34045.1.
- Keranan, K. M., M. Weingarten, G. A. Abers, B. A. Bekins, and S. Ge (2014), Sharp increase in central Oklahoma seismicity since 2008 induced by massive wastewater injection, *Science*, *345*, 448–451, doi:10.1126/science.1255802.
- Lohman, R. B., and W. D. Barnhart (2010), Evaluation of earthquake triggering during the 2005–2008 earthquake sequence on Qeshm Island, Iran, *J. Geophys. Res.*, *115*, B12413, doi:10.1029/2010JB007710.
- Lohman, R. B., and M. Simons (2005), Some thoughts on the use of InSAR data to constrain models of surface deformation: Noise structure and data downsampling, *Geochem. Geophys. Geosyst.*, *6*, Q01007, doi:10.1029/2004GC000841.
- McNamara, D. E., H. M. Benz, R. B. Herrmann, E. A. Bergman, P. Earle, A. Meltzer, M. Withers, and M. Chapman (2014), The *Mw* 5.8 Mineral, Virginia, earthquake of August 2011 and aftershock sequence: Constraints on earthquake source parameters and fault geometry, *Bull. Seismol. Soc. Am.*, *104*(1), 40–54, doi:10.1785/0120130058.
- Meremonte, M. E., J. C. Lahr, A. D. Frankel, J. W. Dewey, A. J. Crone, D. E. Overturf, D. L. Carver, and W. T. Bice (2002), Investigation of an earthquake swarm near Trinidad, Colorado, August–October 2001, *U.S. Geol. Surv. Open File Rep.*, *02-0073*.
- Okada, Y. (1992), Internal deformation due to shear and tensile faults in a half-space, *Bull. Seismol. Soc. Am.*, *82*(2), 1018–1040.
- Rosen, P. A., S. Hensley, G. Peltzer, and M. Simons (2004), Updated repeat orbit interferometry package released, *Eos Trans. AGU*, *85*(5), 47–47, doi:10.1029/2004EO050004.
- Rubinstein, J. L., W. L. Ellsworth, A. McGarr, and H. Benz (2014), The 2001–present triggered seismicity sequence in the Raton Basin of Northern New Mexico and Southern Colorado, *Bull. Seismol. Soc. Am.*
- Sambridge, M. (1999), Geophysical inversion with a neighbourhood algorithm—I. Searching a parameter space, *Geophys. J. Int.*, *138*(2), 479–494, doi:10.1046/j.1365-246X.1999.00876.x.
- Scott, C., R. Lohman, M. Pritchard, P. Alvarado, and G. Sánchez (2014), Andean earthquakes triggered by the 2010 Maule, Chile (*Mw* 8.8) earthquake: Comparisons of geodetic, seismic and geologic constraints, *J. S. Am. Earth Sci.*, *50*, 27–39, doi:10.1016/j.jsames.2013.12.001.
- Wells, D. L., and K. J. Coppersmith (1994), New empirical relationships among magnitude, rupture length, rupture width, rupture area, and surface displacement, *Bull. Seismol. Soc. Am.*, *84*(4), 974–1002.
- Wessel, P., and W. H. F. Smith (1998), New, improved version of generic mapping tools released, *Eos Trans. AGU*, *79*(47), 579–579, doi:10.1029/98EO00426.
- Zhang, Y., et al. (2013), Hydrogeologic controls on induced seismicity in crystalline basement rocks due to fluid injection into basal reservoirs, *Groundwater*, *51*(4), 525–538, doi:10.1111/gwat.12071.